Title

The Interaction between Cu and Fe in P2-Type NaxTMO2 Cathodes for Advanced Battery Performance

Journal

Journal of The Electrochemical Society, 165(7)

ISSN

0013-4651

Authors

Zhang, Yangning
Kim, Sooran
Feng, Guangyuang
et al.

Publication Date

2018

DOI

10.1149/2.0171807jes

Peer reviewed

Journal of The Electrochemical Society, **165** (7) A1184-A1192 (2018)
0013-4651/2018/165(7)/A1184/9/$37.00 © The Electrochemical Society

The Interaction between Cu and Fe in P2-Type Na_xTMO_2 Cathodes for Advanced Battery Performance

Yangning Zhang,[1,2,=] Sooran Kim,[1,=] Guangyuang Feng,[1] Yan Wang,[3] Lei Liu,[3] Gerbrand Ceder,[4,5,*] and Xin Li [1,z]

[1] *John A. Paulson School of Engineering and Applied Sciences, Harvard University, Cambridge, Massachusetts 02138, USA*
[2] *Qiushi Honors College, Tianjin University, Tianjin 300350, People's Republic of China*
[3] *Department of Materials Science and Engineering, Massachusetts Institute of Technology, Cambridge, Massachusetts 02139, USA*
[4] *Materials Science Division, Lawrence Berkeley National Laboratory, Berkeley, California 94720, USA*
[5] *Department of Materials Science and Engineering, University of California, Berkeley, California 94720, USA*

Recently, Cu element has been introduced into layered sodium transition metal oxides (Na_xTMO_2) as cathode materials for sodium ion batteries to engineer rate and cycling performance. To study the unique role provided by Cu, we designed, synthesized and tested four different compositions of P2-type $Na_x(Mn_yFe_zCo_{1-y-z})O_2$ and three compositions of P2-type $Na_x(Mn_yFe_zCu_{1-y-z})O_2$ cathode materials. When cycled in the full voltage range of 1.5∼4.5 V under different rates 0.1 C, 1 C and 10 C, the cyclability of MnFeCu-based compounds is better than that of MnFeCo-based ones. Using X-ray diffraction, we observed the P2 to O2-like phase transition of MnFeCu-based materials upon charging and studied its influence on battery performance. Limiting the P2-O2 phase transition delivers less capacity, but improves cyclability. By DFT simulations, we showed that different Na diffusivity and site preference in the high voltage phase contribute to the difference in the electrochemical performances of these cathode materials.
 [DOI: 10.1149/2.0171807jes]

Manuscript submitted February 5, 2018; revised manuscript received April 9, 2018. Published April 21, 2018.

Sodium-ion batteries have attracted increasing interest due to the natural abundance and low cost of sodium. They are considered to be promising alternatives to lithium-ion batteries for large-scale electric energy storage applications in the near future. Among the many cathode materials for sodium ion batteries, layered sodium transition metal oxides show the highest capacities and energy densities.[1] Layered oxide materials can be categorized into O3 type or P2 type structural groups, in which the sodium ions are accommodated in octahedral and prismatic sites, respectively. Generally, O3 phase compounds exhibit higher average voltage, while the P2 phase compounds show higher capacity and rate capability.[2]

Mn-based and Fe-based P2-type materials are preferred because of their natural abundance and benign environmental impact. P2-$Na_{0.6}MnO_2$[3] reaches a discharge capacity of 140 mAh g^{-1} within the voltage range of 2.0–3.8 V at a current density of 0.1 mA cm^{-2}. The capacity quickly drops to 77% of the 1st cycle after eight cycles. Also, the operating voltage is low due to the low voltage of Mn redox couple. P2-type Na_xFeO_2[4] is unstable and difficult to directly synthesize, because Fe^{4+} cannot be stabilized in the oxide-ion framework under the synthesis conditions. Researchers tried to partially substitute Mn by Fe to stabilize the P2-type phase. Yabuuchi et al.[4] reported P2-$Na_{2/3}Fe_{1/2}Mn_{1/2}O_2$ containing the electrochemically active Fe^{3+}/Fe^{4+} redox couple. This cathode material is reported to deliver a reversible capacity of 190 mAh g^{-1} within the voltage range of 1.5–4.2 V at a current density of 12 mA g^{-1} and good rate capability. With an average voltage of 2.75 V, the energy density is around 520 mWh g^{-1}, which is comparable to some commercial Li-ion battery cathodes. Mortemard de Boisse et al.[5] prepared two P2-phase cathode materials: $Na_{0.67}Mn_{2/3}Fe_{1/3}O_2$ and $Na_{0.71}Mn_{1/2}Fe_{1/2}O_2$, both exhibit discharge capacities between 145–150 mAh g^{-1} within the voltage range of 1.5–3.8 V.

Researchers have also tried to introduce other transition metals such as Co into cathode materials to engineer better rate and cycling performance. Wang et al.[6] studied the electrochemical properties of $P2-Na_{2/3}Mn_yCo_{1-y}O_2$ (y = 0, 1/6, 1/3, 1/2, 2/3, 5/6, and 1) and revealed that with increasing Mn content, the initial discharge capacity increases while the cycle stability degrades. Among them $Na_{2/3}MnO_2$ compound shows the highest initial capacity of 164 mAh g^{-1} in the voltage range of 1.5–4.0 V. Ju-Hsiang Cheng et al.[7] observed that the simultaneous reduction of Co^{3+} and Mn^{4+} to lower valence states during discharge can prevent the monoclinic distortion associated with reduction of Mn^{4+} to Mn^{3+}.

Throne et al.[8] introduced Fe in MnCo-based compounds to maintain the layered crystal structure and synthesized P2-$Na_xMn_{1/3}Fe_{1/3}Co_{1/3}O_2$. When cycled between 1.5–4.0 V, P2-$Na_xMn_{1/3}Fe_{1/3}Co_{1/3}O_2$ has similar initial discharge capacity as P2-$Na_xMn_{1/2}Co_{1/2}O_2$[6] but capacity retention is improved by the use of the Fe^{3+}/Fe^{4+} couple, which is different from their previous observation that Fe^{4+} is a source of capacity fade in $Na_xMn_{1/2}Fe_{1/2}O_2$[9]. When cycled between 1.5–4.5 V, P2-$Na_xMn_{1/3}Fe_{1/3}Co_{1/3}O_2$ exhibits a high initial discharge capacity of 173 mAh g^{-1} and an average voltage of 3.0 V, resulting in 520 mWh g^{-1} energy density. Liu et al.'s work[10] on P2-$Na_{2/3}(Mn_{1/2}Fe_{1/4}Co_{1/4})O_2$ cathode material reported the highest rate performance among layered oxide cathode compounds. The excellent rate performance of this materials is attributed to the wide single P2 phase region and the low Na diffusion barrier.

Taking into account the relative low cost and environmental friendliness of Cu, Cu-based cathode materials are very attractive. Xu et al.[11] utilized the reversible Cu^{2+}/Cu^{3+} redox couple and synthesized air-stable $Na_{0.68}Cu_{0.34}Mn_{0.66}O_2$. When cycled between 2.0–4.3 V, the initial discharge capacity was only 67 mAh g^{-1}. Later, Li et al.[12] added Fe to the compound and synthesized P2-$Na_{7/9}(Mn_{2/3}Fe_{1/9}Cu_{2/9})O_2$. The material exhibits a reversible capacity of 89 mAh g^{-1} within the voltage range of 2.5–4.2 V at 0.1 C rate and an excellent cyclability of 85% after 150 cycles at 1 C rate.

In this paper, we designed and synthesized four different compositions of P2-type $Na_x(Mn_yFe_zCo_{1-y-z})O_2$ cathode materials and three compositions of P2-type $Na_x(Mn_yFe_zCu_{1-y-z})O_2$ cathode materials by solid-state synthesis and tested their electrochemical performance within different voltage windows and under different rates. Especially, we tested the electrochemical performance of all the compounds in the full voltage window of 1.5–4.5 V, within which the largest initial discharge capacity can be achieved, but is often associated with poorer cycling performance compared with narrower voltage window. In MnFeCu-based materials, we observed the phase transition from the P2 phase to an O2-like phase at the high-voltage plateau occurring at ∼4.2 V upon charging using ex-situ X-ray diffraction (XRD), and we investigated its influence on the performance of the cathode materials by Density Functional Theory (DFT) simulations.

There have been a few computational studies on the Na diffusion in the P2 phase and the O2-like phase at the end of charge.[13,14] Na ions in the P2 structure diffuse through a face-shared Na prismatic

=These authors contributed equally to this work.
*Electrochemical Society Member.
[z]E-mail: lixin@seas.harvard.edu

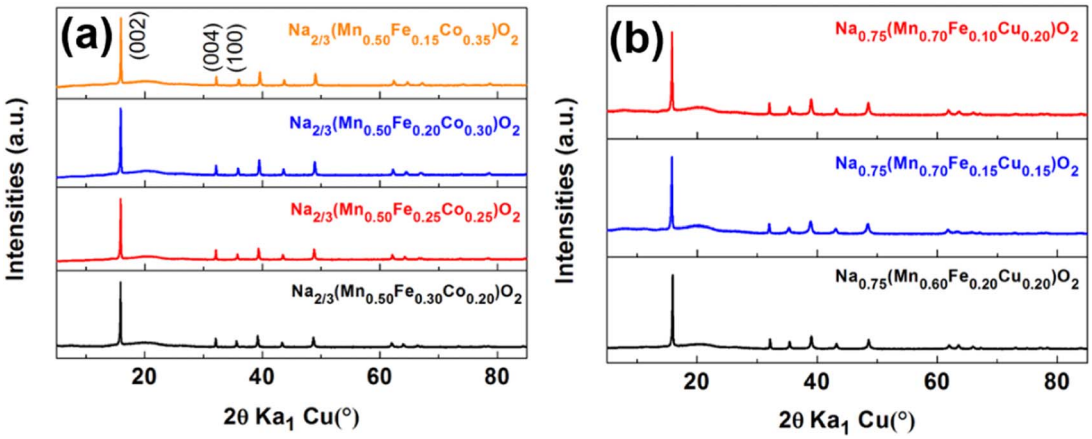

Figure 1. XRD patterns of (a) MnFeCo-based compounds: $Na_{2/3}(Mn_{0.50}Fe_{0.15}Co_{0.35})O_2$, $Na_{2/3}(Mn_{0.50}Fe_{0.20}Co_{0.30})O_2$, $Na_{2/3}(Mn_{0.50}Fe_{0.25}Co_{0.25})O_2$, and $Na_{2/3}(Mn_{0.50}Fe_{0.30}Co_{0.20})O_2$; (b) MnFeCu-based compounds: $Na_{0.75}Mn_{0.70}Fe_{0.10}Cu_{0.20}O_2$, $Na_{0.75}Mn_{0.70}Fe_{0.15}Cu_{0.15}O_2$ and $Na_{0.75}Mn_{0.60}Fe_{0.20}Cu_{0.20}O_2$.

sites in a honeycomb sublattice and in the O2 structure migrate from an octahedral site to another octahedral site through a tetrahedral site. Since the P2 phase in general has a more spacious diffusion pathway, the diffusion barrier is lower than that of the O2 phase. Therefore, the Na diffusion in the O2 phase at the end of charge could be a limiting factor in the charge-discharge process. By building the layered structural models with different local mixtures of transition metal elements such as Fe, Cu, and Co, we try to understand their influence on the battery performance by DFT simulations. We will show from our DFT Nudged elastic band (NEB) calculations that different transition metal (TM) ions can lower the Na diffusion barrier at the end of charge by different degrees and mechanisms. Our results and understanding will guide the design of better cathode materials for sodium ion batteries.

Methods

Synthesis of battery materials.—In the first step of synthesizing MnFeCo-based materials, stoichiometric amounts of Na_2O_2 (97%, Sigma-Aldrich), Mn_2O_3 (99% Sigma-Aldrich), Fe_2O_3 (99.99% Alfa Aesar) and Co_3O_4 (99.7% Alfa Aesar) powder are mixed. For synthesizing MnFeCu-based materials, stoichiometric amounts of Na_2CO_3 (99.95% Alfa Aesar), Mn_2O_3, Fe_2O_3 and CuO (99.90% Sigma-Aldrich) powder are ball-milled. The mixtures are then pressed into pellets and calcined at 900°C in air for 12 h in a tube furnace (the only exception is $Mn_{0.60}Fe_{0.20}Cu_{0.20}$ which was calcined at 860°C). The pellets were quenched to room temperature and transferred immediately into an Ar-filled glove box.

X-ray diffraction measurements.—Both the as-prepared active material and ex-situ cathode films were analyzed by X-ray powder diffraction on a PANalytical X'Pert pro diffractometer equipped with Cu Kα radiation scanned from 10° to 85° 2θ angle. All the samples were sealed carefully with Kapton film to avoid air exposure during the test. Structure analysis using the Rietveld method was carried out by TOPAS.

Electrochemical battery test.—The cathode film was made by mixing 80 wt% of active material, 15 wt% of carbon black (Timcal), and 5 wt% of PTFE (DuPont) as a binder. The mass loading of the cathode film for 0.1 C test is ∼1.9 mg cm^{-2}, for 1 C and 10 C test is ∼1.1 mg cm^{-2}. A Swagelok-type battery was assembled using glass fiber (Whatman GF/F) as a separator, Na metal (99.95% Sigma-Aldrich) as an anode and 1 M NaPF6 (98%, Sigma-Aldrich) dissolved in a mixture of EC:DEC (anhydrous, 1:1 volume ratio) as an electrolyte. The galvanostatic cycling was tested on Arbin BT2000. Prior to cycling, all the pristine cathode films are pre-discharged to 1.5 V at 0.1 C.

Ab initio computation.—All Density Functional Theory (DFT) calculations were performed using the VASP package, which implements the pseudopotential plane wave method.[15,16] The Perdew-Burke-Ernzerhof generalized-gradient approximation (PBE-GGA) was utilized for the exchange-correlation energy.[17] We have performed spin-polarized GGA+U calculations to account for the correlated d electrons of TM ions. The Dudarev method was used for the double-counting correction.[18] The effective on-site correlations, $U_{eff} = U\text{-}J$ are 4.0 eV, 3.9 eV, 5.0 eV, and 3.4 eV for Mn, Fe, Cu and Co, respectively.[19–21]

The space groups of the P2 and O2 phases are $P6_3/mmc$ and $P6_3mc$, respectively.[14] The lattice parameters in the ab plane and atomic positions were fully relaxed without Na ions to model the high voltage phase. The c parameter is fixed to 10 Å for the whole calculations, which is close to the average experimental value of the O2 phase. The spin of Fe and Cu relaxes to the high-spin state whereas that of Co relaxes to the low-spin state. We checked that Cu^{3+} converges to the high-spin state even from the initial low spin state of zero magnetic moment. The energy penalties for TM migration into the sodium layer and for Na migration were calculated in a $4 \times 4 \times 1$ supercell. Only one Na ion was in the supercell for the calculations of the high voltage phase. The composition of the supercell is $Na_{1/32}Mn_{31/32}TM_{1/32}O_2$ (TM = Mn, Fe, Co, or Cu). The electron provided by the only Na ion in the supercell is evenly distributed in the pure Mn case, while it is more localized in the Fe, Co, and Cu doped case when the Na ion is neighboring the doped TM, making their valences below the fully oxidized states. The NEB method is employed to calculate the Na-ion diffusion barrier.[22,23] A gamma centered $2 \times 2 \times 1$ k-point sampling and a 520 eV plane-wave energy cutoff were used for all TM-ion and Na-ion migration calculations.

Results

The XRD patterns of all MnFeCo-based and MnFeCu-based compounds in Fig. 1 can be refined well with the hexagonal space group $P6_3/mmc$ without any diffraction peaks from impurities. It is worth mentioning that for the synthesis of MnFeCu-based compounds, it is difficult to avoid the CuO impurity when the Mn^{4+} content is larger than 0.5. All the patterns are almost identical except for the small shift of the 2θ angle due to the different lattice parameters caused by the different transition metal contents. The lattice parameters of different compositions are shown in Table I. For MnFeCo-based compounds, with the increase of Fe and decrease of Co composition, the a parameter is increasing. This is because the ionic radius of high-spin Fe is larger than that of low-spin Co. However, the c parameter is first increasing and then decreasing with increasing Fe content, indicating that there are other factors competing with ionic radius, such as interplanar interactions. The c parameter

Table I. Refined lattice parameters of as-synthesized samples.

Composition	Lattice Parameter a	Lattice Parameter c	Rwp	χ^2
$Na_{2/3}(Mn_{0.50}Fe_{0.15}Co_{0.35})O_2$	2.879	11.119	2.545	2.809
$Na_{2/3}(Mn_{0.50}Fe_{0.20}Co_{0.30})O_2$	2.885	11.123	2.574	2.816
$Na_{2/3}(Mn_{0.50}Fe_{0.25}Co_{0.25})O_2$	2.895	11.142	2.813	3.028
$Na_{2/3}(Mn_{0.50}Fe_{0.30}Co_{0.20})O_2$	2.905	11.141	3.391	2.419
$Na_{0.75}Mn_{0.70}Fe_{0.10}Cu_{0.20}O_2$	2.920	11.134	3.710	2.377
$Na_{0.75}Mn_{0.70}Fe_{0.15}Cu_{0.15}O_2$	2.926	11.130	3.654	2.621
$Na_{0.75}Mn_{0.60}Fe_{0.20}Cu_{0.20}O_2$	2.924	11.117	3.574	3.203

comparison for MnFeCu-based componds is $c[Na_{0.75}(Mn_{0.70}Fe_{0.10}Cu_{0.20})O_2] > c\ [Na_{0.75}(Mn_{0.70}Fe_{0.15}Cu_{0.15})O_2] > c\ [Na_{0.75}(Mn_{0.60}Fe_{0.20}Cu_{0.20})O_2]$ due to simultaneous change of Mn, Fe and Cu content. If we compare c $(Mn_{0.70}Fe_{0.10}Cu_{0.20})$ and c $(Mn_{0.60}Fe_{0.20}Cu_{0.20})$ which share the same Mn^{4+} and Cu content, it seems that the increasing content of Mn^{3+} plays the most important role in increasing interplanar distance, mostly probably due to the Jahn-Teller (JT) effect of Mn^{3+}.[24]

Fig. 2 shows galvanostatic charge and discharge profiles of MnFeCu-based half cell cycled between 1.5 V and 4.5 V at different rates. When the rate increases from 0.1 C to 1 C and 10 C, the initial capacity drops but the cyclability is improved. For all three compositions at 0.1 C, on the charge curve, there is a high-voltage plateau at 4.2 V and a low-voltage plateau at 2.2 V; on the discharge curve, there is a high-voltage plateau at 3.7 V and a low-voltage plateau at 2 V. Upon cycling, all the plateaus are shortened. Previous work on similar compound shows that the cyclability can be improved significantly if both high and low voltage plateaus are avoided by choosing a narrow voltage window.[12] The discussion here mainly focuses on the change of high-voltage plateau during charge. At 1 C, the high voltage plateau keeps its feature, but is shortened by about 20% compared to 0.1 C for the three Cu based compounds. At 10 C, the plateau almost disappears for $Na_{0.75}(Mn_{0.70}Fe_{0.10}Cu_{0.20})O_2$ and $Na_{0.75}(Mn_{0.70}Fe_{0.15}Cu_{0.15})O_2$, while the plateau is still noticeable for $Na_{0.75}(Mn_{0.60}Fe_{0.20}Cu_{0.20})O_2$.

From Figs. 3a and 3b, the cyclability of MnFeCo-based compounds are very similar in the same voltage window. When cycled between 1.5 V and 4.5 V, the initial capacity is higher but cyclability is worse compared with those cycled between 1.5 V and 4.0 V as the capacity rentention dropped from ~78% to ~59% on average. Figs. 3c and 3d compare the cyclability of MnFeCu-based compounds and $Na_{2/3}(Mn_{0.50}Fe_{0.25}Co_{0.25})O_2$ at 0.1 C in the voltage window of 1.5–4.0 V and 1.5–4.5 V, respectively. Between 1.5–4.0 V, the cyclability of all three MnFeCu-based compounds and $Na_{2/3}(Mn_{0.50}Fe_{0.25}Co_{0.25})O_2$ are quite similar. Also, we can compare their cycling performance in the voltage window of 1.5–4.5 V at different rates 0.1 C, 1 C and 10 C from Figs. 3d, 3e and 3f, respectively. At 0.1 C, $Na_{0.75}(Mn_{0.70}Fe_{0.15}Cu_{0.15})O_2$ has the highest initial capacity but $Na_{0.75}(Mn_{0.60}Fe_{0.20}Cu_{0.20})O_2$ shows the best cyclability. At 1 C, $Na_{0.75}(Mn_{0.70}Fe_{0.15}Cu_{0.15})O_2$ and $Na_{0.75}(Mn_{0.60}Fe_{0.20}Cu_{0.20})O_2$ are very close in capacity and cyclability, both of which are better than $Na_{0.75}(Mn_{0.60}Fe_{0.20}Cu_{0.20})O_2$.

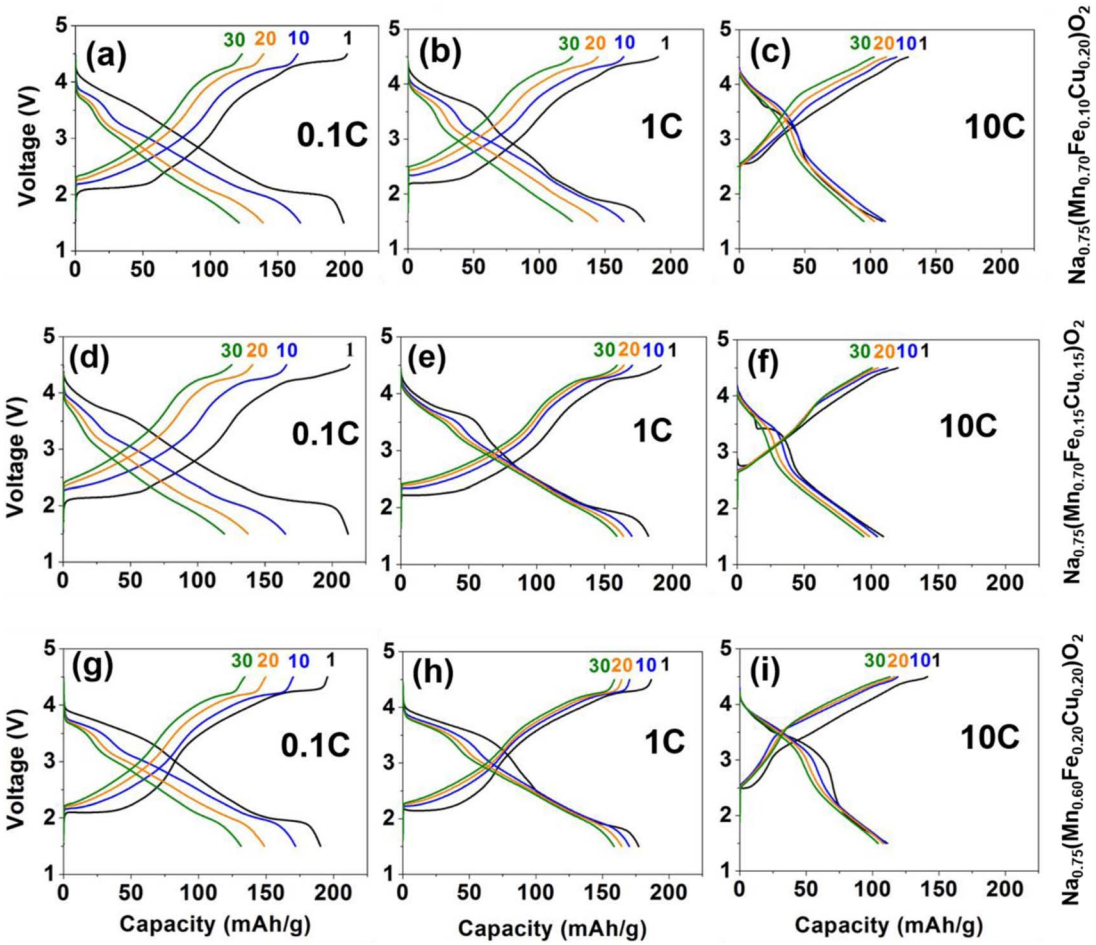

Figure 2. Galvanostatic charge and discharge profiles of MnFeCu-based half cell in 1st, 10th, 20th, 30th cycle: (a)(b)(c) $Na_{0.75}Mn_{0.70}Fe_{0.10}Cu_{0.20}O_2$; (d)(e)(f) $Na_{0.75}Mn_{0.70}Fe_{0.15}Cu_{0.15}O_2$; (g)(h)(i) $Na_{0.75}Mn_{0.60}Fe_{0.20}Cu_{0.20}O_2$; (a)(d)(g) tested at 0.1 C rate; (b)(e)(h) tested at 1 C rate; (c)(f)(i) tested at 10 C rate. All is predischarged to 1.5 V and then cycled between 1.5 V and 4.5 V.

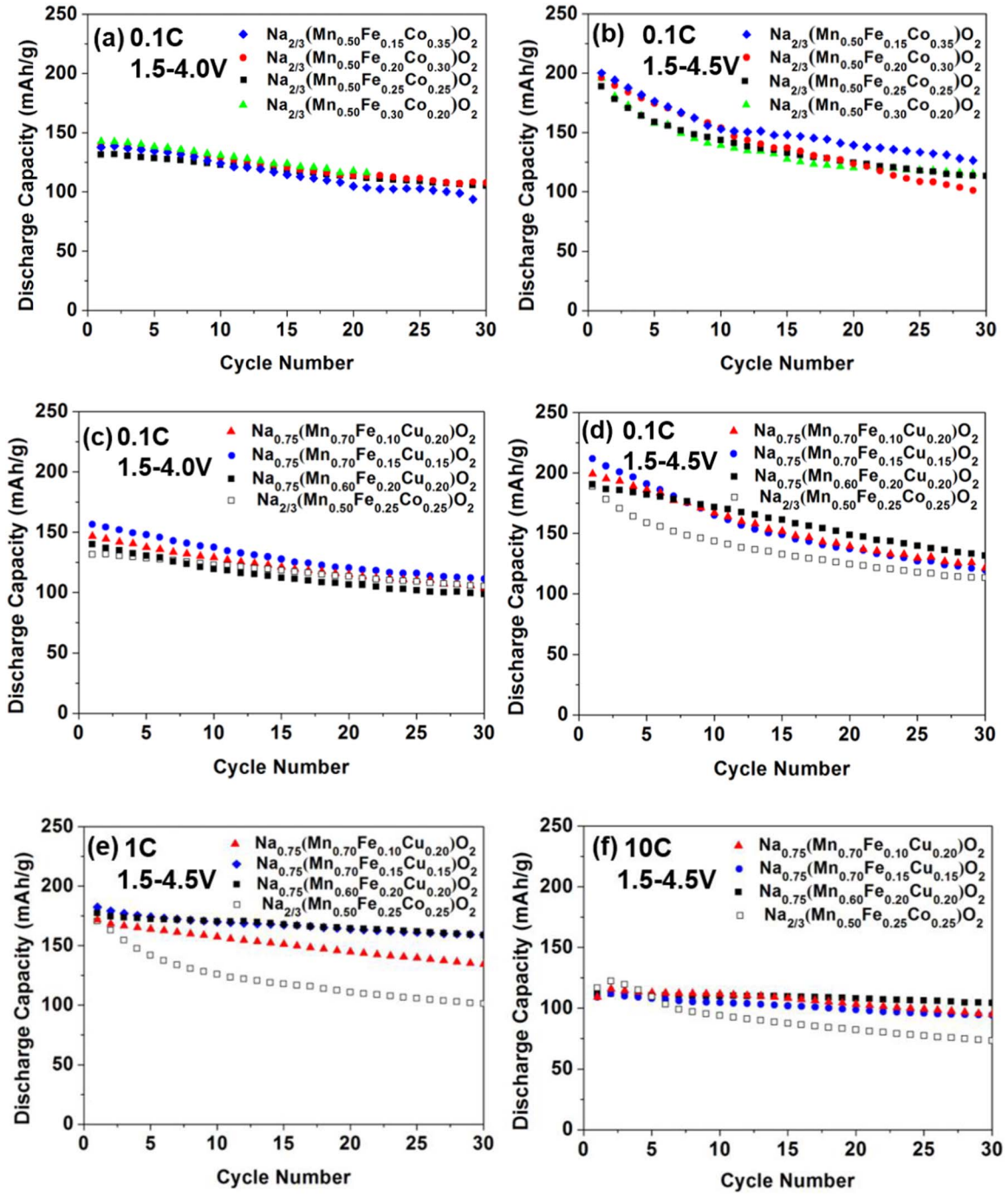

Figure 3. Cyclability of MnFeCo-based and MnFeCu-based compounds at different voltage window and rates: (a) MnFeCo-based compounds cycled at 0.1 C between 1.5 V and 4.0 V; (b) MnFeCo-based compounds cycled at 0.1 C between 1.5 V and 4.5 V; (c) MnFeCu-based compounds and $Na_{2/3}(Mn_{0.50}Fe_{0.25}Co_{0.25})O_2$ cycled at 0.1 C between 1.5 V and 4.0 V; (d) MnFeCu-based compounds and $Na_{2/3}(Mn_{0.50}Fe_{0.25}Co_{0.25})O_2$ cycled at 0.1 C between 1.5 V and 4.5 V; (e) MnFeCu-based compounds and $Na_{2/3}(Mn_{0.50}Fe_{0.25}Co_{0.25})O_2$ cycled at 1 C between 1.5 V and 4.5 V; (f) MnFeCu-based compounds and $Na_{2/3}(Mn_{0.50}Fe_{0.25}Co_{0.25})O_2$ cycled at 10 C between 1.5 V and 4.5 V.

At 10 C, the initial capacity of MnFeCu-based compounds are almost the same but $Na_{0.75}(Mn_{0.60}Fe_{0.20}Cu_{0.20})O_2$ shows slightly better cyclability. In addition, at all rates between 1.5–4.5 V, the cyclability of three MnFeCu-based compounds are better than that of $Na_{2/3}(Mn_{0.50}Fe_{0.25}Co_{0.25})O_2$. Quantitatively, the average capacity rentetion of MnFeCu-based compounds compared with the capacity retention of $Na_{2/3}(Mn_{0.50}Fe_{0.25}Co_{0.25})O_2$ are 62% v.s. 59% at 0.1 C, 82% v.s. 60% at 1 C, and 87% v.s. 62% at 10 C, respectively.

Fig. 4 compares the rate performance of each MnFeCu-based compound. For all three compounds, as the rate increases from 0.1 C to 1 C and 10 C, the initial capacity decreases. With increasing rates, the cyclability is improved for $Na_{0.75}(Mn_{0.70}Fe_{0.10}Cu_{0.20})O_2$ from 61% at 0.1 C to 69% at 1 C and 85% at 10 C, while for both $Na_{0.75}(Mn_{0.70}Fe_{0.15}Cu_{0.15})O_2$ and $Na_{0.75}(Mn_{0.60}Fe_{0.20}Cu_{0.20})O_2$, the cyclability at 1 C and 10 C are very close, and both are better than at 0.1 C.

Fig. 5 shows the ex-situ XRD patterns of MnFeCu-based cathode films at different charge and discharge states (pristine, 1.5 V at predischarge end, and 4.5 V at charge end). For all three compositions, when the pristine cathode films (black) are pre-discharged to 1.5 V (blue),

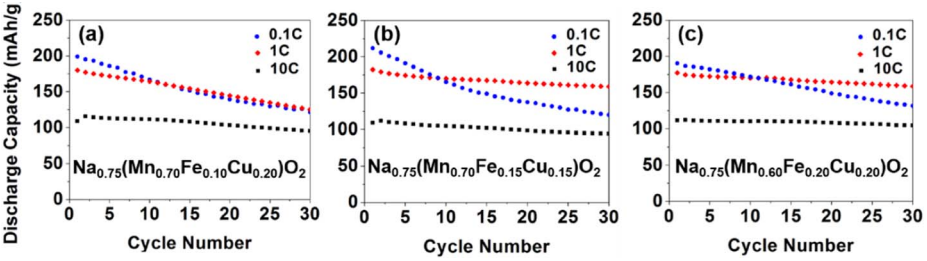

Figure 4. Rate performance of MnFeCu-based compounds cycled at 0.1 C, 1 C and 10 C between 1.5 V and 4.5 V: (a) $Na_{0.75}Mn_{0.70}Fe_{0.10}Cu_{0.20}O_2$; (b) $Na_{0.75}Mn_{0.70}Fe_{0.15}Cu_{0.15}O_2$; (c) $Na_{0.75}Mn_{0.60}Fe_{0.20}Cu_{0.20}O_2$.

the XRD patterns maintain the characteristic P2 peaks quite well. However, the (002) and (004) peaks are asymmetrical and broader, and several additional peaks occur in 2θ angles between 30° and 70° after pre-discharging, indicating the formation of a two-phase structure for fully sodiated MnFeCu through the low voltage plateau. After predischarging to 1.5 V and then charging to 4.5 V (red), the (002) peak shifts to larger 2θ angle, with decreased intensity and broadened width. What is more obvious is that almost all the characteristic P2 peaks between 30° and 50° disappear with only one small peak left at around 36°. In Rietveld refinement, the experimental XRD pattern for charged MnFeCu can be refined with the O2 model (hexagonal space group $P6_3mc$[14]). Detailed Rietveld refinement results are listed in Table II. For the fully sodiated MnFeCu patterns, we only performed the single phase refinement on the major P2 phase because the other phase only shows very weak peaks in XRD, which does not allow a two phase refinement.

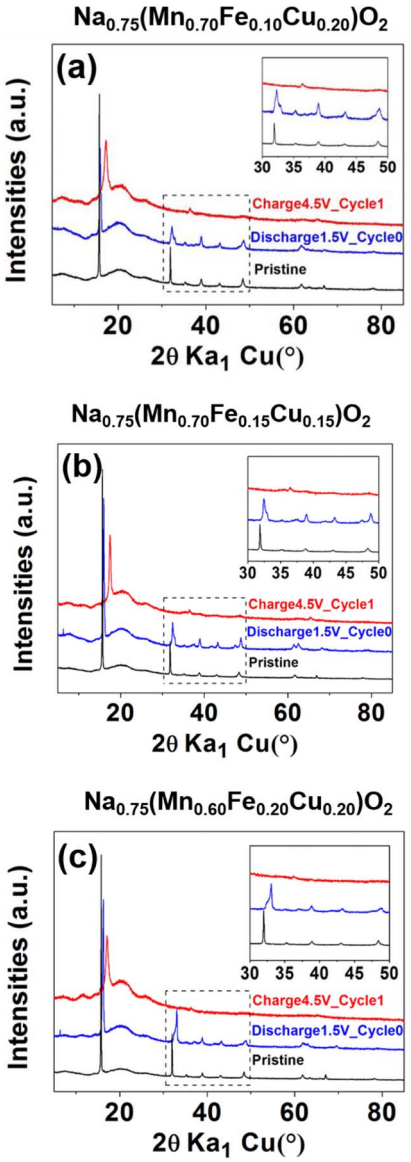

Figure 5. Ex-situ XRD patterns of MnFeCu cathode films at different voltage: (a) $Na_{0.75}Mn_{0.70}Fe_{0.10}Cu_{0.20}O_2$; (b) $Na_{0.75}Mn_{0.70}Fe_{0.15}Cu_{0.15}O_2$; (c) $Na_{0.75}Mn_{0.60}Fe_{0.20}Cu_{0.20}O_2$. Red: the cathode film pre-discharged to 1.5 V and then charged to 4.5 V at 0.1 C; blue: the cathode film pre-discharged to 1.5 V at 0.1 C; black: the pristine cathode film. Inset: enlarged XRD patterns in 2θ angles between 30° and 50°.

Fig. 6 compares the ex-situ XRD patterns of MnFeCu-based cathode films discharged to 1.5 V at different rates after 30 cycles with the pre-discharged ones. For all three MnFeCu compositions, the cathode films maintain the P2 structure quite well when they are cut off at 1.5 V after cycling at 1 C (red) and 10 C (black) for 30 times. However, when cycled at 0.1 C and cut off at 1.5 V, most peaks are not symmetrical for both the pre-discharged samples (green) and the samples after 30 cycles (blue). The phenomenon that both the (002) and (004) peaks of these 0.1 C tested samples show superposition of at leaset two peaks further supports the coexistence of two phases. Higher rate tests at 1 C and 10 C largely avoid the low voltage plateau (Fig. 2) associated phase transition toward this two-phase region, hence maintain the P2 phase upon cycling. This is different from P2- $Na_{2/3}(Mn_{0.50}Fe_{0.25}Co_{0.25})O_2$ where no such two-phase region is observed upon discharging to low voltage even at 0.1 C.[10] Detailed Rietveld refinement results of these XRD patterns are listed in Table II.

According to Table II, all compositions are pre-discharged to 1.5 V, and then cycled between 1.5–4.5 V at different rates after 30 cycles. The *c* parameters for 1 C and 10 C cycled samples are very close, and both are larger than at 0.1 C. This is most probably caused by the larger amount of Na vacancy left in the 1 C and 10 C tested samples. The residue Na vacancy is due to the incomplete discharge associated with high rate.

Based on the shift of (002) peak upon discharging and charging, we further probe the correlation between the structural change of $Na_x(Mn_{0.60}Fe_{0.20}Cu_{0.20})O_2$ with Na content in Fig. 7. The samples are cutoff at different voltages (1.5 V at pre-discharge end, 3.4 V, 4.1 V and 4.5 V upon charging) during first cycle at 0.1 C followed by ex-situ XRD. The XRD patterns ofpristine, 1.5 V and 4.5 V cathode films are shown in Fig. 5c. At each state, the corresponding Na content can be calculated under the assumption that at the end of initial discharge the Na content is near 100%. Thus, we are able to correlate the lattice parameter c with Na content, as shown in Fig. 7. When Na is extracted from the structure, the *c* parameter slightly increases until *x* approaches 0.4 and then decrease drastically due to P2-O2 phase transition until $x \sim 0.2$ corresponding to 4.5 V charge. A similar change of the *c* parameter with the Na composition is also observed in the other two MnFeCu based compounds and previously reported P2 materials such as $Na_x[Ni_{1/3}Mn_{2/3}]O_2$[14], $Na_{2/3}(Mn_{1/2}Fe_{1/4}Co_{1/4})O_2$[10], $Na_xFe_{0.5}Mn_{0.5}O_2$[25,26], and $Na_{2/3}[Mg_{0.28}Mn_{0.72}]O_2$[27], and is generic for many alkali-layered oxides such as Li_xCoO_2.[28,29]

Discussion

Battery performance overview.—As shown in Figure 3, at 0.1 C, the initial discharge capacity of MnFeCu-based compounds is higher than $Na_{2/3}(Mn_{0.50}Fe_{0.25}Co_{0.25})O_2$, while at 1 C and 10 C, they are

Table II. Rietveld refinement results (lattice parameters and R-factors).

Composition	Voltage	Rate	Cycle	Lattice Parameter		R_{wp}
				a	*c*	
$Na_{0.75}Mn_{0.70}Fe_{0.10}Cu_{0.20}O_2$		10 C	30	2.913	11.182	5.245
	1.5 V	1 C		2.917	11.172	4.706
		0.1C		2.922	11.079	5.273
			0	2.924	11.044	4.726
$Na_{0.75}Mn_{0.70}Fe_{0.15}Cu_{0.15}O_2$		10 C	30	2.920	11.172	5.505
	1.5 V	1 C		2.910	11.239	4.276
		0.1C		2.923	11.020	5.216
			0	2.926	10.958	5.024
$Na_{0.75}Mn_{0.60}Fe_{0.20}Cu_{0.20}O_2$		10 C	30	2.914	11.181	4.094
	1.5 V	1 C		2.925	11.160	4.707
		0.1C		2.945	11.070	5.234
			0	2.959	10.787	6.572

very similar. When cycled between 1.5 V and 4.5 V at all rates, the cyclability of MnFeCu-based compounds are better than that of $Na_{2/3}(Mn_{0.50}Fe_{0.25}Co_{0.25})O_2$. With an initial discharge capacity of 224 mAh g^{-1} and an average discharge voltage of 2.63 V, the initial discharge energy density of $Na_{0.75}(Mn_{0.70}Fe_{0.15}Cu_{0.15})O_2$ can reach 592 mWh g^{-1}, much larger than $Na_{2/3}Fe_{1/2}Mn_{1/2}O_2$ materials[4] with an energy density of 520 mWh g^{-1}.

Li et al.[12] introduced Cu into P2-type cathode materials and achieved excellent cyclability at 1 C in the voltage window of 2.5–4.2 V to avoid the high-voltage plateau. In our tests, we expand the voltage window to 1.5–4.0 V and 1.5–4.5 V in order to investigate the effect of the high and low voltage phases on the battery performance rather than optimizing the best cycliability and capacity. Actually, we also tested the MnFeCu-based half-cells between 2.5–4.0 V, and such narrow voltage window did provide us with better cyclability, which is probably due to the exclusion of the Jahn-Teller Mn^{3+}.[10,24] Since the lower rates provide orders of magnitude longer time for the battery to stay at high voltage range compared with the higher rates, the effect of any high voltage related capacity fading mechanism, such as electrolyte decomposition, will be magnified at lower rates. However, our results also show the importance of intrinsic difference in the cathode compounds to the capacity fading, such as shown in Figure 3d. We will show that the major intrinsic difference in the electrochemical performances of these cathode can be explained by different Na diffusivity and site preference in the high voltage phase.

O2-like phase at high voltage plateau.—Previous reports also observed the high-voltage plateau of P2-phase materials upon charging and identified it as phase transition from P2 to certain new phases such as O2[14], OP4[4] or double-layer O2[25] phase. Lee et al.[14] investigated the reversible phase transition from P2 to O2 in P2-$Na_x[Ni_{1/3}Mn_{2/3}]O_2$ ($0<x<2/3$) materials by ex-situ synchrotron XRD and first principles calculations. They discovered that the *c* parameter decreased drastically at the phase change region. Excellent cycling properties and high rate capability can be obtained by excluding the P2–O2 phase transformation. The observed SXRD patterns of $Na_x[Fe_{1/2}Mn_{1/2}]O_2$ at 4.2 V[4], however, were fitted by neither the O2 phase nor P2 phase. Instead, the pattern was explained by assuming the formation of the OP4 phase with stacking faults, in which the octahedral and prismatic layers are piled up alternately along the *c*-axis direction. Talaie et al.[25] studied the structural evolution of P2-$Na_{0.67-z}Fe_{0.5}Mn_{0.5}O_2$ (where z~0.5) upon cycling and solved the crystal structure of the high voltage phase by X-ray pair distribution function analysis. The double-layer O2 model they proposed agreed with the measured PDF of the high-voltage phase. Liu et al.[10] and Boisse et al.[26] also referred to the unidentified high-voltage phase as Z phase in FeMn-based compounds. Despite the different high voltage structures in the literature, they all contain certain structural component with the O2 stacking.

In our study, the phase transition generally occurs when charged to 4.2 V and above at 0.1 C for both MnFeCo and MnFeCu based systems. This corresponds to a Na content of ~40% for MnFeCu-based compounds and a Na content of ~34% for MnFeCo-based ones.[10] In Rietveld refinement, our XRD patterns at 4.5 V can be refined by the O2 model with hexagonal space group $P6_3mc$[14] better than with the OP4 and double-layer O2 model. Therefore, we assume that for our MnFeCu-based compounds, the high voltage plateaus on charge and discharge profiles correspond to a phase transition from P2 to an O2-like phase. From our XRD results, the drastic decrease of *c* parameter associated with the P2-O2 phase transition reveals the decrease of interslab distance upon Na extraction.

Including the high-voltage plateau in the electrochemical test can deliver more capacity, but usually leads to worse cyclability. With increasing rates from 0.1 C to 1 C and 10 C, the plateau shortens (or even disappears for $Na_{0.75}(Mn_{0.70}Fe_{0.10}Cu_{0.20})O_2$ and $Na_{0.75}(Mn_{0.70}Fe_{0.15}Cu_{0.15})O_2$ at 10 C) and the cyclability is improved, which gives further evidence that limiting P2-O2 transition can improve the cyclability. This is consistent with the better cyclability obtained with a 4.0 V charge cutoff than with a 4.5 V cutoff. The capacity fading at high voltage cutoff could be partly caused by electrolyte decomposition.[30] But as we show below, different site perferencce and Na diffusivity in the high voltage O2 phase are the two other factors that dominate the different electrochemical performance in these compounds.

Na-ion diffusivity and its interaction with TM ion.—The O2-like phase at the end of charge likely limits Na-diffusivity since the Na-ion diffusion barrier of the O2 phase is higher than that of the P2 phase,[13,14] and its significantly decreased lattice parameter *c* from ~11.5 Å to ~9.5 Å (Figure 7) can reduce the Na ion diffusivity. This effect could either reduce the capacity or decrease the cyclability when the O2-P2 transition is included in the voltage window. Thus, we focus on the Na diffusion barrier in the O2 structure where the transition metal difference would have a larger influence on the Na ion diffusivity than that in the P2 structure.

Figure 8 shows results from the DFT nudged elastic band calculations on the Na migration barrier in the O2 with different TM ions in the diffusion pathway. A Na ion migrates from an octahedral site to another octahedral site through a tetrahedral site in the O2 structure as shown in the insets of Fig. 8,[14] and its activation energy is strongly controlled by the interaction of the Na in the tetrahedral site with the face-sharing TM-ion, similar to the previous study on the high voltage O3 phase.[31] The diffusion barrier for the pure Mn compound is lowered when the TMO_6 octahedron that is face-sharing with the tetrahedral Na site is occupied by Fe, Cu, or Co. The migration barriers are summarized in Table III.

We have previously shown that the buckling of the oxidized Fe in high voltage O3 phase leads to a lower migration barrier for Na.[31]

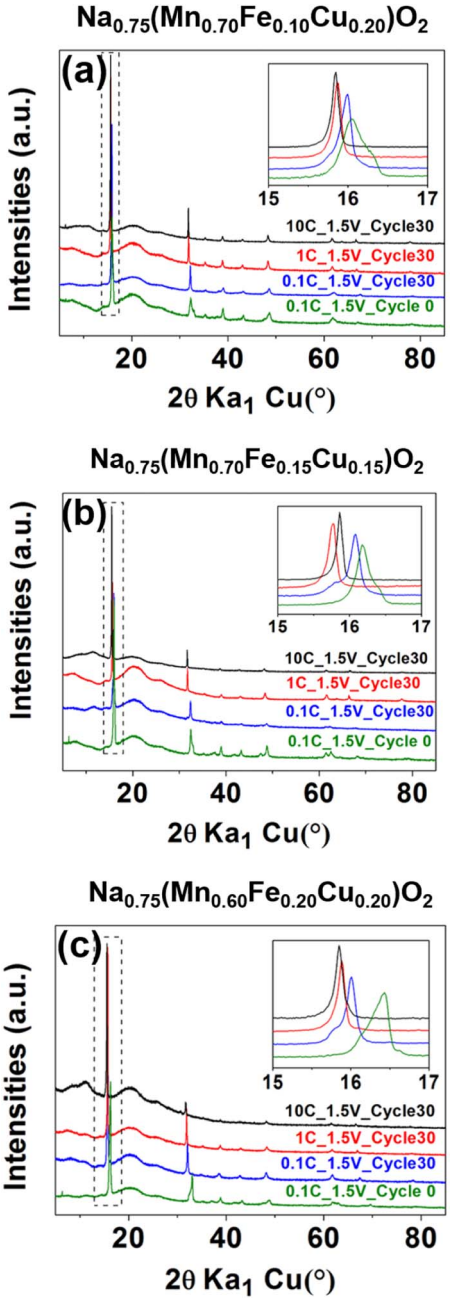

Figure 6. Ex-situ XRD patterns of MnFeCu compositions cut off at 1.5 V after cycling between 1.5–4.5 V at different rates: (a) $Na_{0.75}Mn_{0.70}Fe_{0.10}Cu_{0.20}O_2$; (b) $Na_{0.75}Mn_{0.70}Fe_{0.15}Cu_{0.15}O_2$; (c) $Na_{0.75}Mn_{0.60}Fe_{0.20}Cu_{0.20}O_2$. Black: the cathode film cycled at 10 C for 30 times and cut off at 1.5 V; red: the cathode film cycled at 1 C for 30 times and cut off at 1.5 V; blue: the cathode film cycled at 0.1 C for 30 times and cut off at 1.5 V; green: the pristine cathode film predischarged to 1.5 V at 0.1 C. Inset: enlarged (002) peaks in 2θ angles between 15° and 17°.

Similarly in our high voltage O2 phase, when a Na ion passes through the tetrahedral site, a buckling of the Fe-O bond is detected as shown in the lower center inset of Fig. 8. The distance between Na and Fe is increased by the Fe buckling, resulting in lower Na diffusion barrier. Interestingly, Cu and Co ions also reduce the Na diffusion barrier, but do not show the buckling behavior during the Na migration, so that their effect on the barrier must operate through another mechanism than the buckling mechanism with the oxidized Fe. Our Bader analysis shows that Cu and Co have about 0.5 more electrons than the oxidized Mn and Fe, making the net Bader charge or the nominal valence of

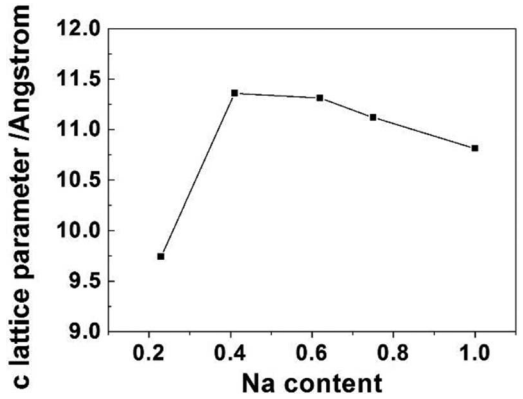

Figure 7. The *c* lattice parameter at different Na content for $Na_{0.75}Mn_{0.60}Fe_{0.20}Cu_{0.20}O_2$. The Na content at the five data points each corresponds to a cutoff voltage (from left to right: 0.23 mol for charging to 4.5 V, 0.41 mol for charging to 4.1 V, 0.62 mol for charging to 3.4 V, 0.75 mol for pristine, and 1 mol for pre-discharging to 1.5 V).

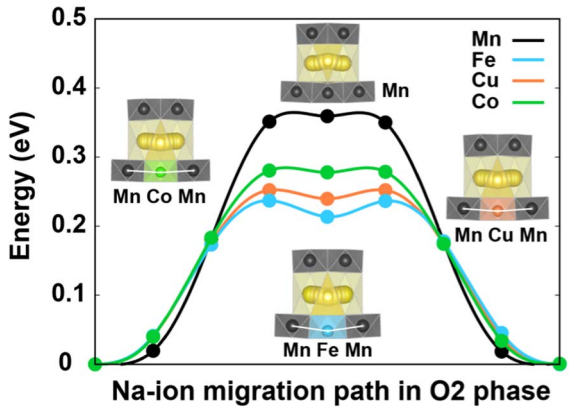

Figure 8. Na-ion migration paths and barriers in the O2 phase. Insets depict the Na-ion migration path for each doped TM ion. Black, blue, orange, and green balls represent Mn, Fe, Cu, and Co, respectively. The lower center inset depicts the buckling of Fe.

Cu (1.31) and Co (1.41) lower than Mn (1.89) and Fe (1.90), while the Na net Bader charge is always around 0.89 in these four cases at the transient site. The lower valency reduces the Coulombic repulsion between Na^+ and Cu or Co ions, resulting in a lower Na-ion diffusion barrier similar to what has been argued for layered Li-oxdies.[28,32] Note the oxidized Cu is close to high-spin Cu^{3+} without JT distortion. Therefore, the lowest diffusion barrier of Fe case has to be explained by the soft Fe-O bonding associated buckling mechanism.[31] This can also be seen from the angles of Mn-X-Mn bonds (X = Mn, Fe, Co, or Cu; Mn is with face-sharing pathway for this comparison) indicated by the white line in Fig. 8, where the angles are 171.7°, 163.1°, 174.8° and 171.4° for X = Mn, Fe, Co and Cu, respectively, corresponding to the Na-TM distance of 2.73 Å, 2.83 Å, 2.62 Å and 2.67 Å, respectively. The smallest angle and largest buckling of TM (i.e. largest Na-TM distance) is seen in the Fe case.

Table III. Diffusion barriers depending on the type of TM ions in Na diffusion pathway.

	Diffusion barrier depending on the TM ion (eV)			
c parameter (Å)	Mn	Fe	Cu	Co
10.00	0.36	0.24	0.25	0.28
9.081	0.71	0.54	0.59	0.66

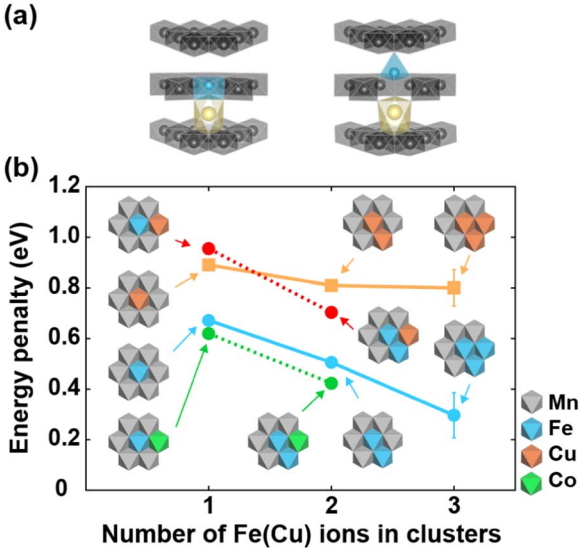

Figure 9. (a) Model systems for TM migration. Left and right ones represent before TM migration and after TM migration into the sodium layer, respectively. (b) Energy penalties for the TM migration depending on the composition of TM ions. The migrated ion, Fe or Cu is located in the center of each cluster. Error bars indicate the standard deviation from the different configuration with same number of doped TM ions in the cluster.

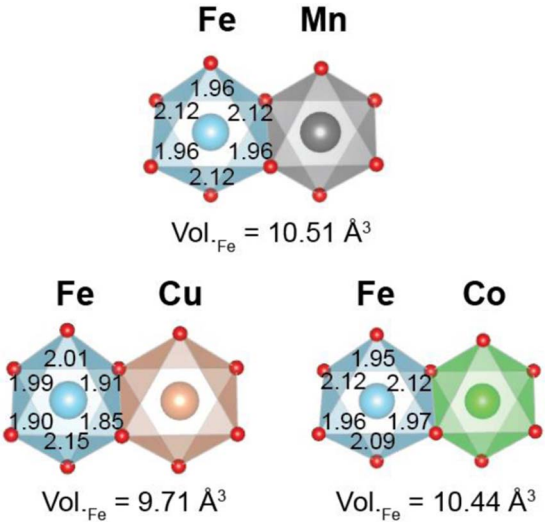

Figure 10. FeO_6 octahedron volume and Fe-O bond length (in Å) depending on the neighboring TM ion.

Based on the above arguments, our DFT simulations show that the Na ion energetically prefers the diffusion pathway without face-sharing with Mn in the pure Mn case (Fig. 8), due to the strong electrostatic repulsion from Mn ion. The doped ions of Fe, Co, Cu reduced the energy barriers of the face-sharing diffusion pathways due to different mechanisms, making them energetically favorable than the ones without face-shaing. Thus TM ion doping would be helpful to reduce the Na ion diffusion barrier in the high voltage O2-like phase, especially when the interslab distance is small at the end of charge.

Increased Fe migration energy penalty by Cu doping in O2 phase.—TM migration into the alkali metal layer can cause capacity loss,[33] or lower alkaline ion diffusivity,[28] leading to poor cyclability. The TM migration barrier depends on the type and composition of TM ions.[31,34] When a TM migrates from an octahedral site in the TM layer into a tetrahedral site in the Na layer (Figure 9a), their energy difference is referred as the energy penalty for TM migration. Fig. 9b shows the energy penalty for different TM ions with different neighboring configurations in the O2 structure. The insets in Fig. 9b show the ion configuration in each local TM cluster, where the center ions are always the migrated ions of Fe or Cu.

Both isolated Fe or Cu ions have relatively high energy penalty of 0.67 eV and 0.89 eV, respectively. The energy penalty for the Fe migration drops significantly as forming the Fe cluster (the blue solid line in Fig. 9b), similar to previous finding in the O3 structure. However, we find that the Cu local clusters show clearly different behaviors on the TM migration from the Fe cluster. The energy penalty for the Cu migration in the Cu cluster is similar to that of an isolated Cu (the orange solid line in Fig. 9b). Therefore, Cu does not suffer from the clustering induced TM migration as in the Fe cluster case.

The reduced energy cost of the Fe migration in the Fe cluster can be understood through the JT effect of the oxidized Fe.[31] We have analyzed the relaxed structures containing the local Fe (or Cu) clusters. Fe^{4+} ions in the cluster all show strong JT distortion, which provide the structural distortion needed for Fe sitting in the migrated tetrahedral site in the Na layer and collectively lower the energy cost for the migration. In contrast, our simulations shows that JT and non-JT Cu ions coexist in the local Cu cluster. The charge disproportionation of Cu ions assembles the structurally distorted and non-distorted CuO_6 octahedral together in the Cu cluster, which inhibits the structural distortion for Cu migrating to the tetrahedral site in the Na layer.

Furthermore, the energy penalty for a TM migration is also strongly influenced by the type of its neighboring TM ions. For the Fe migration, when one of its six neighboring Mn ions is replaced by a Cu (the red dotted line in Fig. 9b), or a Co (the green dotted line in Fig. 9b) atom, the calculated energy penalites for a Fe migration are very different. Our result shows that a neighboring Cu ion can significantly stabilize the neighboring Fe ion or ion clusters, whereas a neighboring Co ion cannot. We find that when Fe is located beside Cu, the charge transfer happens from Fe to Cu due to the larger electronegativity of Cu. With neighboring Cu ion, both the Fe-O bond length and volume of Fe octahedron reduce noticeably compared with neighboring Mn or Co cases as shown in Figure 10. The shortened Fe-O bond length with neighboring Cu significantly enhances the energy penalty and effectively prevents the Fe migration into the sodium layer. In contrast to the Cu case, the Fe-O bond length and Fe octahedral volume embedded in Mn clusters almost keep their values, when a Co ion locates beside a Fe ion. In other words, the effect of Co ions on the Fe migration is similar to that of Mn ion. These results agree with the experimental result in Fig. 3. The worse performance of MnFeCo than that of MnFeCu can be partly caused by higher probability of Fe migration in the high voltage O2-like phase in the compound with Co.

Conclusions

In conclusion, we demonstrated through a combination of electrochemical test, ex-situ XRD measurement, and first principles calculations that Cu can be substituent in layered P2-type $NaTMO_2$ cathode materials to improve the electrochemical performance of sodium ion batteires. P2-type $Na_x(Mn_yFe_zCu_{1-y-z})O_2$ cathode materials show better cyclibility than P2-type $Na_x(Mn_yFe_zCo_{1-y-z})O_2$ materials within the full voltage range of 1.5∼4.5 V at all rates, 0.1 C, 1 C and 10 C. We studied the transition from P2 to O2-like phase of MnFeCu-based materials at high voltage and confirmed with DFT simulations that the Na ion diffusivity in the high voltage phase is improved by Cu and Fe doping. It is worth mentioning that a Cu cluster in the O2 structure is much more resistant to TM migration than a Fe cluster. Furthermore, a neighboring Cu ion can stabilize the Fe cluster whereas Co ion cannot. This work highlights the possibility of using Cu in P2-type cathode materials to improve Na ion diffusivity and TM layer stability. Our understanding will hopefully stimulate further studies on the design of better cathode materials.

Acknowledgments

This work is supported by computational resources from the Extreme Science and Engineering Discovery Environment (XSEDE) and the Odyssey cluster supported by the FAS Division of Science, Research Computing Group at Harvard University. Y. Z. acknowledges the support from the Undergraduate Thesis Research Training Program funded by Tianjin University. S. K. acknowledges the support from Basic Science Research Program through the National Research Foundation of Korea (NRF) funded by the Ministry of Education (2016R1A6A3A03007900).

ORCID

Xin Li https://orcid.org/0000-0001-9390-0830

References

1. R. J. Clément, P. G. Bruce, and C. P. Grey, *J. Electrochem. Soc.*, **162**, A2589 (2015).
2. M. H. Han, E. Gonzalo, G. Singh, and T. Rojo, *Energy Environ. Sci.*, **8**, 81 (2014).
3. A. Caballero, L. Hernán, J. Morales, L. Sánchez, J. Santos Peña, and M. A. G. Aranda, *J. Mater. Chem.*, **12**, 1142 (2002).
4. N. Yabuuchi, M. Kajiyama, J. Iwatate, H. Nishikawa, S. Hitomi, R. Okuyama, R. Usui, Y. Yamada, and S. Komaba, *Nat. Mater.*, **11**, 512 (2012).
5. B. M. de Boisse, D. Carlier, M. Guignard, and C. Delmas, *J. Electrochem. Soc.*, **160**, A569 (2013).
6. X. Wang, M. Tamaru, M. Okubo, and A. Yamada, *J. Phys. Chem. C*, **117**, 15545 (2013).
7. J.-H. Cheng, C.-J. Pan, J.-F. Lee, J.-M. Chen, M. Guignard, C. Delmas, D. Carlier, and B.-J. Hwang, *Chem. Mater.*, **26**, 1219 (2014).
8. J. S. Thorne, R. A. Dunlap, and M. N. Obrovac, *J. Electrochem. Soc.*, **161**, A2232 (2014).
9. J. S. Thorne, R. A. Dunlap, and M. N. Obrovac, *J. Electrochem. Soc.*, **160**, A361 (2012).
10. L. Liu, X. Li, S.-H. Bo, Y. Wang, H. Chen, N. Twu, D. Wu, and G. Ceder, *Adv. Energy Mater.*, **5**, 1500944 (2015).
11. S.-Y. Xu, X.-Y. Wu, Y.-M. Li, Y.-S. Hu, and L.-Q. Chen, *Chinese Phys. B*, **23**, 118202 (2014).
12. Y. Li, Z. Yang, S. Xu, L. Mu, L. Gu, Y.-S. Hu, H. Li, and L. Chen, *Adv. Sci.*, **2**, 1500031 (2015).
13. Y. Mo, S. P. Ong, and G. Ceder, *Chem. Mater.*, **26**, 5208 (2014).
14. D. H. Lee, J. Xu, and Y. S. Meng, *Phys. Chem. Chem. Phys.*, **15**, 3304 (2013).
15. G. Kresse and J. Furthmüller, *Phys. Rev. B*, **54**, 11169 (1996).
16. G. Kresse and J. Furthmüller, *Comput. Mater. Sci.*, **6**, 15 (1996).
17. J. P. Perdew, K. Burke, and M. Ernzerhof, *Phys. Rev. Lett.*, **77**, 3865 (1996).
18. S. L. Dudarev, G. A. Botton, S. Y. Savrasov, C. J. Humphreys, and A. P. Sutton, *Phys. Rev. B*, **57**, 1505 (1998).
19. S. P. Ong, V. L. Chevrier, G. Hautier, A. Jain, C. Moore, S. Kim, X. Ma, and G. Ceder, *Energy Environ. Sci.*, **4**, 3680 (2011).
20. G. Hautier, S. P. Ong, A. Jain, C. J. Moore, and G. Ceder, *Phys. Rev. B*, **85**, 155208 (2012).
21. S. Lany, *Phys. Rev. B*, **87**, 85112 (2013).
22. H. Jónsson, G. Mills, and K. W. Jacobsen, *Class. Quantum Dyn. Condens. Phase Simulations*, 385 (1998).
23. G. Henkelman and H. JoŕNsson, *J. Chem. Phys.*, **113**, 9978 (2000).
24. X. Li, X. Ma, D. Su, L. Liu, R. Chisnell, S. P. Ong, H. Chen, A. Toumar, J. Idrobo, Y. Lei, J. Bai, F. Wang, J. W. Lynn, Y. S. Lee, and G. Ceder, *Nat. Mater.*, **13**, 586 (2014).
25. E. Talaie, V. Duffort, H. L. Smith, B. Fultz, and L. F. Nazar, *Energy Environ. Sci.*, **8**, 2512 (2015).
26. B. M. de Boisse, D. Carlier, M. Guignard, L. Bourgeois, and C. Delmas, *Inorg. Chem.*, **53**, 11197 (2014).
27. N. Yabuuchi, R. Hara, K. Kubota, J. Paulsen, and S. Komaba, *J. Mater. Chem. A*, **2**, 16851 (2014).
28. K. Kang and G. Ceder, *Phys. Rev. B*, **74**, 94105 (2006).
29. A. Van der Ven, M. K. Aydinol, G. Ceder, G. Kresse, and J. Hafner, *Phys. Rev. B*, **58**, 2975 (1998).
30. S. Komaba, N. Yabuuchi, T. Nakayama, A. Ogata, T. Ishikawa, and I. Nakai, *Inorg. Chem.*, **51**, 6211 (2012).
31. X. Li, Y. Wang, D. Wu, L. Liu, S. Bo, and G. Ceder, *Chem. Mater.*, **28**, 6575 (2016).
32. K. Kang, Y. S. Meng, J. Breger, C. P. Grey, and G. Ceder, *Science*, **311**, 977 (2006).
33. J. P. Peres, C. Delmas, A. Rougier, M. Broussely, F. Perton, P. Biensan, and P. Willmann, *J. Phys. Chem. Solids*, **57**, 1057 (1996).
34. S. Kim, X. Ma, S. P. Ong, and G. Ceder, *Phys. Chem. Chem. Phys.*, **14**, 15571 (2012).